

Long-term Microglial Phase-specific Dynamics During Single Vessel Occlusion and Recanalization

xiaoke xie

xiexie_ke@zju.edu.cn

Xuanting Liu

Zhejiang University

Yiwen Chen

Zhejiang University

Jiazhu Zhu

Zhejiang University

Yongxian Xu

Zhejiang University

Xiaojing Li

Zhejiang University

Yameng Zheng

Zhejiang University

Shangyue Gong

Zhejiang University

Xiao Xiao

Zhejiang University

Jianmin Zhang

Zhejiang University

Wei Gong (✉ weigong@zju.edu.cn)

Zhejiang University <https://orcid.org/0000-0001-5568-5930>

Ke Si

Zhejiang University

Article

Keywords: Vessel Occlusion, Recanalization, spatiotemporal

Posted Date: December 8th, 2021

DOI: <https://doi.org/10.21203/rs.3.rs-1112810/v1>

License:  This work is licensed under a Creative Commons Attribution 4.0 International License.

[Read Full License](#)

Version of Record: A version of this preprint was published at Communications Biology on August 19th, 2022. See the published version at <https://doi.org/10.1038/s42003-022-03784-0>.

Abstract

Vascular occlusion leading to brain dysfunctions is usually considered evoking microglia-induced inflammation response. However, it remains unclear how microglia interact with blood vessels in the development of vascular occlusion-related brain disorders. Here, we illuminate long-term spatiotemporal dynamics of microglia and their activation pattern during single vessel occlusion and recanalization. The results show that microglia display remarkable response characteristics in different phases, including acute reaction, rapid diffusion, transition and chronic effect. Microglial cell body represents a unique filament-shape migration and has slower motility compared to the immediate reaction of processes to occlusion. We capture single microglia with few processes moves out of the cluster and redistributes territory with increasing ramified processes. Microglial cluster resolves gradually until microglial number and morphology become stabilized. Therefore, our study offers a comprehensive analysis of spatiotemporal dynamics of microglia to both vessel occlusion and recanalization. Microglial phase-specific response suggests the morphological feature-oriented phased intervention would be an attractive option for vascular occlusion-related diseases treatments.

Introduction

Vascular occlusion, as one of the primary causes of disability, is implicated in multiple disease factors (Cruz Hernandez et al., 2019; Tennant & Brown, 2013; Zhang et al., 2020). Previous studies suggest that vascular occlusion leads to neural deficits, infarction and cognitive dysfunctions (Lubart et al., 2021; Shih et al., 2013; Summers et al., 2017). Vascular occlusion evokes inflammation response in the brain (Chamorro, Dirnagl, Urra, & Planas, 2016; Moskowitz, Lo, & Iadecola, 2010; S. Xu, Lu, Shao, Zhang, & Zhang, 2020). However, the mechanism of the interaction between the vascular occlusion and inflammation response is not fully elucidated. As the main effectors of the innate inflammatory response in the central nervous system (CNS), microglia have been extensively studied in vascular occlusion-related diseases (Cortes-Canteli et al., 2019; Fernandez-Lopez et al., 2016; Liu et al., 2021; Lubart et al., 2021; Mastorakos et al., 2021; Neumann et al., 2015; Szalay et al., 2016; Zhou et al., 2017).

Microglia are regarded as one of the most important immune defense lines in the CNS (Andoh & Koyama, 2021; Greenhalgh, David, & Bennett, 2020; Nayak, Roth, & McGavern, 2014; Prinz, Jung, & Priller, 2019). They are highly active in the intact brain, constantly survey their territory as well as interact with other cortical elements (Bernier et al., 2020; Mendes et al., 2021; Nimmerjahn, Kirchhoff, & Helmchen, 2005). Microglia processes extend toward the excitotoxicity neuron after cerebral ischemia to decrease excitotoxic injury in a P2Y₁₂ receptor-dependent manner through altered somatic junctions (Cserep et al., 2020; Szalay et al., 2016). In addition to microglia-neuron interaction (Cangalaya, Stoyanov, Fischer, & Dityatev, 2020; Lim & Ruthazer, 2021; Umpierre et al., 2020; Umpierre & Wu, 2020), the correlation between microglia and blood vessels has drawn increasing attention in the pathological progression of occluded vascular dysfunctions (Dudvarski Stankovic, Teodorczyk, Ploen, Zipp, & Schmidt, 2016; Jolivel et al., 2015; Neumann et al., 2015; Qiu et al., 2021). Blood vessels bring adequate oxygen and glucose delivery, which are required for microglia function and viability. Using the photothrombotic approach, researchers

found that the activity of microglia is affected by the blood flow near its cell body, rather than the microenvironment around distal microglial processes (Masuda, Croom, Hida, & Kirov, 2011). Microglia perform phagocytosis leading to vascular disintegration in the middle cerebral artery occlusion (MCAO) treated mouse (Fu, Shen, Xu, Luo, & Tang, 2014; Jolivel et al., 2015). However, the traditional vessel occlusion operations, such as photothrombotic and MCAO model, are limited by the dysfunction resulting from multiple vascular occlusion and inherently activated microglia (induced by *in vitro* slicing procedure). These factors would intervene the morphological analysis of microglia. The functional performance of microglia is closely associated with changes in its morphology and motility, thus the specific morphological structure or displacement could indicate microglial functional activities. The function of microglia in extending processes is impaired with P2RY12 receptors inhibition (Mastorakos et al., 2021). Microglia migrate to the contralateral hemisphere through the corpus callosum after cortical microinfarcts in a CX3CR1-dependent manner to affect remote brain regions reorganization (Lubart et al., 2021). Moreover, microglia form clusters following genetic ablation to achieve repopulation (Bruttger et al., 2015). To explore the function of microglia in neurological diseases, it is necessary to investigate the temporally precise microglia morphological dynamics in diverse blood vessels microenvironment *in vivo*.

Currently, most study of microglia dynamics properties and transformation mechanisms focus on a certain morphological change of microglia during the acute reaction phase. Microglial rapid chemotactic response is regulated by extracellular adenosine triphosphate (ATP) released from damaged tissue and nearby astrocytes after the laser microlesion in the brain parenchyma (Davalos et al., 2005; Mastorakos et al., 2021). Microglia converge on the laser microlesion site, forming a rounded protective barrier to prevent brain damage from further spreading (Hines, Hines, Mulligan, & Macvicar, 2009). However, the microglial complicated spatiotemporal morphological transformation characteristics are not well investigated in the long-term scale. Here, we applied laser ablation technique (Nishimura et al., 2006) to occlude single vessels and performed long-term *in vivo* imaging with two-photon laser scanning microscope (TPLSM) to investigate the response of microglia during both vessel occlusion and recanalization phase. We describe the microglia dynamics with four different phases: acute reaction, rapid diffusion, transition and chronic effect during the long-term imaging process. These findings give insights into the spatiotemporal dynamics of microglia during vessel occlusion and recanalization, which might lay the foundation on modulating microglial activities for vascular occlusion-related diseases treatments.

Results

Establishment of single vessel occlusion in CX3CR1-GFP mouse

We applied laser ablation technique to occlude the single vessel to performed long-term *in vivo* imaging of microglia response. Before making single vessel occlusion model, we did cranial window implantation above the mouse cortex (Fig. 1A). As the primary immune effector cells in the brain, microglia are activated and their morphology changes with functional transformations in response to any kind of brain damage or injury. To eliminate surgery-induced effects on the morphology of microglia, we performed

long-term imaging after cranial window implantation to record microglia and blood flow state influenced by the surgery. After the surgery, we imaged the morphology of microglia on the same FOV for up to a month continuously (Supplementary Fig. 1A). According to the process tree area and the blood flow velocity results (Supplementary Fig. 1B, C), about 4-weeks recovery before the single vessel occlusion is necessary for ruling out the influence factor brought by cranial window implantation. Additionally, increases in imaging quality over time can be observed on the same FOV at day 25, and the morphology of microglia had the appearance of ramified processes (Supplementary Fig. 1A).

Subsequently, we made the model of single vessel occlusion. The targeted vessel was imaged with *in vivo* two-photon microscope (Fig. 1B), which relied on contrast generated by labeling the blood plasma with Texas Red. The vessels diameters varied from 5 μm to 100 μm . We chose the vessel with diameter of ~ 20 μm and depth of ~ 80 μm from the pia as the targeted vessel. Insult to the targeted vessel was generated by irradiation of the lumen of the vessel with a laser at the wavelength of 1070 nm (Fig. 1B). This process provided real-time feedback on the progress of vessel diameter and blood flow velocity changing (Supplementary Fig. 2). When a single vessel is occluded, the clotted site was full of accumulated nonfluorescent RBCs, which was visualized as a dark lump within the vessel (Supplementary Fig. 2A). It is worth noting that the appropriate laser power should be set to avoid hemorrhage by vessel rupture (Supplementary Fig. 3).

Long-term *in vivo* imaging of microglia and blood vessel after vessel occlusion

We imaged the dynamics of microglia caused by laser-induced vascular occlusion for more than 70 days. In this process, microglia experienced morphological transformation from aggregation mass to diffusion individual. According to the dynamic characteristics, we divided the whole pathological process into four phases: acute reaction phase (0-24 h), rapid diffusion phase (day 1-day 5), transition phase (day 5-day 31) and chronic effect phase (\geq day 32) (Fig. 2A).

We employed relative fluorescence intensity of occlusion core-centered different areas (X, Y, Z) to quantify microglia response to vessel occlusion from the inner area to the outer area (Fig. 2B). Results demonstrate that the closer to the occlusion core, the higher the fluorescence intensity of the microglia (Fig. 2C). Beginning with a general polynomial curve fitting of fluorescence intensity changes over time, we found fluorescence intensity changes can be roughly divided into increasing and decreasing periods. To investigate theoretically possible mechanism of microglial phase-specific dynamics, we used S-curve (Peleg & Corradini, 2011; P. Xu, 2020) and diffusion-consumption equation (Marinov & Santamaria, 2014; Oyler-Yaniv et al., 2017) to fit our data. In the acute reaction phase, fluorescence intensity shows an S-curve-like increasing tendency. Subsequently, the diffusion-consumption equation was used to fit fluorescence intensity data accompanied by recanalization. According to the fitting curve, results show that fluorescence intensity of area X increased dramatically in the acute reaction phase with the average change rate of fluorescence intensity is 634.18 ($\Delta F/F$)/day (Fig. 2D). Previous study demonstrates that the release of nucleotides is one of the important reasons for the aggregation of microglia (Haynes et al., 2006). We speculate that occlusion leads to the release of related cytokines, and these cytokines make

microglia quickly gather towards the occlusion core. After the surrounding microglial sensors are occupied, the release of more cytokines cannot increase microglial chemotaxis and the fluorescence intensity reaches the maximum at this time. In the rapid diffusion phase, fluorescence intensity of occlusion core decreased (Fig. 2D). The average change rate of fluorescence intensity of area X, area Y and area Z is 119.45, 34.16 and 2.11 ($\Delta F/F$)/day, respectively. This suggests that microglial diffusion rate is much slower compared with its rapid aggregation. In the transition phase, the average change rate of fluorescence intensity of area X, area Y and area Z is 5.24, 1.69 and 0.41 ($\Delta F/F$)/day, respectively. In the chronic effect phase, the average change rate of fluorescence intensity of area X, area Y and area Z is 0.41, 0.17 and 0.08 ($\Delta F/F$)/day, respectively. These results indicate that as time increases, the decrease rate of fluorescence intensity slows down, that is, the microglial density decreases until it stabilizes. Considering the diffusion-consumption mechanism (Oyler-Yaniv et al., 2017), we speculate that when microglial fluorescence intensity is at a high level and in a rapid decline stage, the spatial spread size of diffusion-effect cytokines is small. On the contrary, diffusion-effect cytokines display a big spatial spread. At the same time, we observed that the blood flow began to recover spontaneously about 1.5 days after occlusion. Unexpectedly, blood flow velocity has been in a fluctuating state in the following days, accompanied by vascular malformation (Supplementary Fig. 4).

Microglia dynamics in the acute reaction phase

Microglia outgrew processes immediately after vessel occlusion, which became obvious 20 minutes later (Supplementary Fig. 5A). A hollow spherical containment, which was reported as a protective barrier preventing damage from spreading around (Hines et al., 2009), had been formed around the occlusion site 60 minutes after occlusion. This hollow appearance was also consistent with what was shown in the MCAO model, since few microglia present inside the ischemic core (Gelosa et al., 2014). The processes of the nearby microglia reached the clotted site, forming a solid spherical containment within 250 minutes (Supplementary Fig. 5A). During this phase, we found microglia activation based on the distance to the clotted site, from near to far, which took place sequentially. The five microglia showed in Figure 3A are named as microglia 1, 2, 3, 4, 5, respectively. Their location was as shown in Supplementary Figure 5A. Microglia 1 was the nearest to the occlusion site, microglia 5 the farthest. We employed T-index to quantitatively analyze the degree of microglia activation (Fig. 3B). Before the occlusion, all the five microglia had the appearance of normal morphology with ramified processes. When the blood vessel was blocked, the nearest microglia 1 elongated its occlusion facing process and its non-occlusion facing process retracted at the same time. But the other four microglia retained their ramified processes. In the next few hours, microglia 2 gone through this transition 100 min post occlusion, 130 min for microglia 3, 250 min for microglia 4, 350 min for microglia 5, respectively (Fig. 3A). T-index significantly correlated with time after occlusion (Supplementary Fig. 5B), which demonstrates the activation degree of microglia increasing over time.

Compared with T-index at 720-780 min, T-index at 24 h increased significantly (Fig. 3C, $P < 0.0001$), which suggests that the process elongation state has ended 24 h after occlusion. At the same time, the core of solid spherical containment got the most microglia aggregation, while the microglia aggregation in the

area far away from the core is greatly reduced (Supplementary Fig. 5C, relative intensity: X = 415.89 ± 68.70 , Y = 132.04 ± 21.93 , Z = 25.95 ± 2.90).

Although microglial processes responded very quickly, microglial cell bodies motility response was much slower. We found cell bodies migration was performed in two distinct ways (Fig. 4A-C), including the cell bodies deformation migration and cell bodies non-deformation migration. Cell bodies deformation migration was named filamentous-like movement (Fig. 4A). In this way, the cell body was stretched into filaments and then migrated into the occlusion core. Cell bodies non-deformation migration were divided into two categories. The first category underwent obvious displacement (Fig. 4B), and cell body in another category vanished while adjacent cell bodies kept stationary (Fig. 4C). The cumulative motility was only $2.52\% \pm 1.51$ at 100-120 min after occlusion (Fig. 4D), which suggests the majority of cell bodies keep stationary during this phase. However, the cumulative motility rate increased rapidly reaching $76.71\% \pm 3.89\%$ at 720-780 min. Cumulative motility rate was $86.87\% \pm 3.89\%$ at 24 h and suggests that almost all microglia have been translocated. In previous reports, few studies have mentioned the movement of the microglia cell body. Here, our results provide an accurate and concise clarification about it.

Microglia dynamics in the rapid diffusion phase

After having known the characteristics of the acute response of microglia to vessel occlusion, we repeatedly imaged to investigate what happens to the microglia after cluster formation. At this phase, we can see massed outlines of microglial cell bodies with few short processes around the occlusion core at day 1 (Fig. 5A). Then these cell bodies continued to move out of the core, and the process began to be abundant until the majority of them finally became the ones with normal symmetrical process at day 5.

Due to the removal of the cell bodies from the core, the relative fluorescence intensity of the occlusion core decreased from 608.23 ± 220.98 at day 1.5 to 150.42 ± 62.00 at day 5 (Fig. 5B). Unexpectedly, no obvious fluctuation was observed in the intensity of the outer area from the occlusion core, which means that the emerged microglia migrated continuously to the remote area to maintain a balance of spatial distribution. The total number of microglia in the FOV also gradually increased, from 34.67 ± 1.86 at day 1 to 55.67 ± 2.73 at day 5 (Fig. 5C). In terms of morphology, we found that the microglia were still activated at day1 (Fig. 5D) with T-index 0.79 ± 0.05 , followed by a significant increase in the T-index at day 1.1 (Fig. 5E, 0.96 ± 0.05 , $P < 0.01$). No significant difference in T-index was observed from day 1.1 to day 5, which indicates the morphology of microglia has been stable.

In addition to cell bodies moving out from the occlusion core, we found that the proliferation of microglia also contributed to the increased microglial number. Our imaging described in detail microglial proliferation procedure (Fig. 5F, top). At the same time, microglia disappeared in their original position and also appeared in the original blank position (Fig. 5F, middle and bottom). Through these various morphological changes discussed above, the microenvironment within the FOV was renewed.

Microglia dynamics in the transition phase and chronic effect phase

Next, we continued to study the microglia dynamics in the later phases of vascular occlusion. During the transition phase, although accumulation of perivascular microglia decreased (Fig. 6A), microglia density was still slightly higher in proximity to occlusion core. Therefore, the relative fluorescence intensity of occlusion core was significantly higher than that of the outer area (Fig. 6B). In terms of microglia number, it decreased significantly at day 28-31 (46.00 ± 3.00) compared with that at day 5-6 (53.43 ± 1.93) (Fig. 6C). There was no difference in the morphology of microglia (Fig. 6D). These results show that the pathological effects caused by vascular occlusion still exist in the transition phase.

In the chronic phase, microglial cluster resolved (Fig. 6E). There was no significant difference of relative fluorescence intensity between inner area and outer area (Fig. 6F). Microglial cell number and morphology T-index within the FOV also showed no obvious fluctuations (Fig. 6G, H). Therefore, perivascular microenvironment presented stability in the chronic phase to a certain extent.

Discussion

In this paper, we explore the *in vivo* spatiotemporal dynamics of microglia during single vessel occlusion and recanalization up to 73 days. We find that there are four phases of distinct microglia dynamics characteristics, including acute reaction, rapid diffusion, transition and chronic effect. In the acute reaction phase (0-24 h), microglia are rapidly activated manifested by processes elongation towards occluded sites as expected. Furthermore, we identified the morphological changes and diverse displacement of cell bodies that occur much later compared to that of processes. In the rapid diffusion phase (day 1-day 5), single microglia move out of the cluster, which leads to decreasing in fluorescence intensity of occlusion core and increasing in microglial number. In the transition phase (day 5-day 31), microglia cluster still exist, since fluorescence intensity of occlusion core is significantly higher than that of distant area. Finally, relative fluorescence intensity, cell number and cell morphology of microglia no longer exhibit significant fluctuations in the chronic phase (\geq day 32). Compared with previous research focused on the acute reaction phase, our study well investigated the microglial complicated morphological transformation characteristics in the long-term scale.

It is worth noting that microglia processes are the main participants moving toward to injury site in the acute reaction phase. By tracking the same microglia, we demonstrate that the motility of microglial cell bodies did not start to increase positively until 120 min after the occlusion. Since imaging sessions also has a certain time interval, we found that a small part of the cell bodies, either close to the occlusion core or becoming filamentous ones, could migrate into the occlusion core. Rapid increasing in cumulative mobility is primary contributed by the disappearance of the cell body, so it is ambiguous that whether the cell bodies have migrated to the occlusion core. Strikingly, in the rapid diffusion phase, we found plenty of microglia with clear round shape cell body move out from the cluster. We speculate that microglial proliferation occurs during the phase of interaction between microglia cluster and occluded vessel. In a previous genetic cell ablation study, many microglial micro-clusters are found at around day 7, and

mostly resolve by day 14 (Bruttger et al., 2015). These formed clusters prove to be highly proliferative, and single cells migrate away from the cluster once steady state is achieved. IL-1R on microglia participates in this cluster-style proliferation process. This research strongly supports our speculation. Besides, consistent with the previous observation, the cluster resolved to redistribute single microglia territory to regulate brain parenchyma microenvironment. Furthermore, combining pharmacologically manipulating these redistributed proliferation cells, such as cell depletion, with more advanced optical methods (Fan et al., 2020), it is expected to illuminate their role in the subsequent long-term pathological development.

It has been reported in acute experimental research that ATP mediates a rapid microglial chemotaxis requires P2Y receptor through either its associated potassium channels activation or extracellular nucleotides (Haynes et al., 2006; Wu, Vadakkan, & Zhuo, 2007). However, the chemotaxis mechanism of microglia is not the same in different models of neurological diseases, and the detrimental or protective role of microglia remains highly controversial in neurological diseases (Cherry, Olschowka, & O'Banion, 2014; Fu et al., 2014; Gelosa et al., 2014; Prinz & Priller, 2014). In autoimmune encephalomyelitis mice, it is blood protein fibrinogen that induces rapid microglial responses toward the vasculature leading to axonal damage (Davalos et al., 2012; Merlini et al., 2019). Whereas, under the pathological blood brain barrier (BBB) breakdown condition, perivascular microglial processes play a protective role in the maintenance of BBB integrity following cerebrovascular damage (Lou et al., 2016). Additionally, it is particularly important that microglia respond to ischemic injury dynamically. The microglia experience an early neuroprotective M2 phenotype, followed by a transition to a proinflammatory M1 phenotype (Hu et al., 2015; Hu et al., 2012), which suggests corresponding treatments for different pathological phases should be considered. In particular, the changes in microglial morphology are closely related to microglial functional transformations (Fumagalli, Ortolano, & De Simoni, 2014). Therefore, our finding of specific morphological dynamics involved in different phases, suggests using different methods (including pharmaceutical and optogenetics) to modulate microglial activities at different pathological phases will strongly support us to further research on functions and mechanisms mediated by microglial morphology.

Materials And Methods

Transgenic mice

Heterozygous CX3CR1^{GFP/+} mice were used for all experiments. In these mice, microglia are labeled with an enhanced green fluorescent protein (EGFP), which provides high contrast in microglia soma and processes imaging. The animals were housed in a temperature-controlled and humidity-controlled room with a 12h/12h light/dark cycle. Mice were allowed free access to purified water. The appropriate guidelines for the care and use of laboratory animals were approved by the Committee for Animal Experiments of Zhejiang University.

Implantation of chronic cranial window

Transgenic CX3CR1^{GFP/+} mice (8 to 10 weeks old) were anesthetized with isoflurane (1.5%-2.5%) and placed in a stereotactic frame with a heating pad (36-37.5 °C). Depth of anesthesia was assessed by monitoring pinch withdrawal and respiration rate. Eyes were protected with ointment.

The scalp was incised with scissors. Lidocaine (2%) was administered locally. Then we carefully removed the muscle and connective tissue above skull with a disposable blade or needle. A small craniotomy (approximately 3 mm × 3 mm) was performed using a high-speed drill with a small-tip steel burr (0.5 mm in diameter), centered at 1.7 mm lateral to the midline and 2 mm posterior to bregma. A double-layered coverslip consisted of a small coverslip (3 mm in diameter) attached to a large one (6 mm in diameter), which was embedded and sealed with dental cement. The small layer fitted snugly into the craniotomy, and the large one was attached to the polished skull.

The last step used dental cement to fix the head plate on the skull. The mice were placed on a heating pad until they were fully awake. Antibiotics injections were administered after surgery for at least one week. Mice were housed for about 4-weeks recovery from the surgery.

***In vivo* long-term imaging with a two-photon microscope**

EGFP-labeled microglia were imaged by a two-photon microscope through a small craniotomy as described above. By raster scanning a femtosecond-pulsed laser beam (Chameleon Ultra II, Coherent) via standard galvanometer raster scanning with a moving *in vivo* microscope (Bruker Corporation), two-photon imaging was performed. A 16×/0.8-NA water-immersion objective (Nikon) was used in all the experiments. The Ti-sapphire laser was set at the excitation wavelength of 920 nm for both EGFP-expressing microglia and Texas red-labeling blood vessels imaging. A stack of image planes (1064 × 1064 pixels) with a step size of 2 μm was acquired using the water-immersion objective at a zoom of 2.0. The maximum imaging depth was ~350 μm from the pial surface. Images were acquired with low laser power (< 50 mW at the sample).

To visualize the vasculature and the motion of red blood cells (RBCs) with TPLSM, we injected 7 mg/kg Texas Red dextran (70000 MW, neutral; Thermo) in 0.9% NaCl intravenously. Line scans were used along single vessels with a maximum scan rate of 5 kHz to quantify RBCs velocity. RBCs movement resulted in dark diagonal streaks in the image with a slope that was inversely proportional to the RBCs velocity.

Vascular occlusion with two-photon laser

The excitation source for the photostimulation path was a femtosecond-pulsed laser fixed at 1070 nm (total output, 2 watts; pulse width, 55 fs; Coherent). We focused a two-photon laser beam (~15 μm in diameter) on the vessel through the cranial window to create a highly localized injury, and the laser power was set at 80–200 mW. The photostimulation beam was paused at the anticipated position of the vessel for approximately 1–30 s to create a small injury site, which was indicated by a bright fluorescent circle around the focal point of the beam. We assessed blood flow and vascular appearance from the real-time

TPLSM images to adjust the laser power, and pulse duration until the final establishment of vascular occlusion.

Data analysis

Images were processed by ImageJ software. All z-stacks of images were projected along the z-axis to produce two-dimensional maximum intensity projection images within the imaged volumes. Function as a morphological parameter, the microglial territory areas were quantified by circumscribing the outline of the ends of microglia processes with a smooth polygon tool in ImageJ.

To account for signal intensity differences that arose from different long-term imaging experiments, microglia fluorescence image was separated from the two-channel images and then signal intensity measurements were conducted. We measured microglia fluorescence intensity changes through four concentric circles from the inner area to the outer area (X, Y, Z), and the fourth outermost circle was regarded as baseline fluorescence value F_0 . We measured the mean gray value in each circle as $F(t)$. The relative fluorescence intensity of all the circular area was therefore given by $\Delta F/F = (F(t) - F_0(t))/F_0(t) \times 100$.

The blood vessels were loaded with fluorescent dyes that imaging the outline of perfused vessels. RBCs were displayed as dark particles in the bright background. RBCs velocity were measured with MATLAB 2016a (MathWorks, USA). Vessel diameter and morphology analysis were measured manually with ImageJ.

To evaluate the changes in microglia morphology, we quantitatively analyzed the transitional stage morphology index (T-index) (Eles et al., 2017). The T-index was calculated based on the length of the longest microglia process facing the injury blood vessel (n) and the length of the longest microglia process facing away from the injured blood vessel (f). The morphology index was therefore given by $T\text{-index} = (f - n)/(f + n) + 1$. Lastly, Imaris software was applied to assess microglia morphology three-dimensional reconstruction.

For cell bodies cumulative motility analysis, we analyzed microglia in the field of view (FOV) within a volume of $410.55 \mu\text{m} \times 410.55 \mu\text{m} \times 20 \mu\text{m}$. Individual microglia was identified and marked with numbers before vessel occlusion. If the cell bodies maintain their position by comparing the surrounding landmark objects (such as blood vessels), they are considered to be static, or if they are not present or exist in a position greater than $10 \mu\text{m}$ based on the previous image, they are considered to be migrating. Cumulative motility was determined as the number of migratory cells divided by the total number of cells before occlusion $\times 100\%$.

Curve fitting of microglial fluorescence intensity changes

S-curve (Ding, Li, Lin, Kimochi, & Sudo, 2017; P. Xu, 2020) and diffusion-consumption equation (Marinov & Santamaria, 2014; Oyler-Yaniv et al., 2017) were used to fit the fluorescence intensity changes over time.

The S-curve equation is:

$$F_1(t) = \frac{A}{1+Be^{-\gamma t}} \quad (1)$$

where $F_1(t)$ (fluorescence intensity) is the dependent variable for the S-curve, t is the time, B and γ are model parameters, while A is the carrying density of microglia in this study.

Immune response-induced cytokine diffusion and consumption is governed by a diffusion-consumption mechanism (Oyler-Yaniv et al., 2017). Fluorescence intensity has a power function relationship with time. We thus modified the equation as follows:

$$F_2(t) = \frac{K}{(t+\Delta t)^2} + C \quad (2)$$

where $F_2(t)$ (fluorescence intensity) is the dependent variable, t is the time, K , Δt and C are model parameters.

The parameter values of the two equations of X, Y, Z (from the inner area to the outer area based on occlusion core) are shown in Table 1. The fitting curves were smoothly using algorithm processing.

Table 1. Parameter values for curves fitting in our experiment

Area	A	B	γ	K	Δt	C
X	612.00	23.00	9.28	1950.00	0.47	50.00
Y	180.00	23.13	8.04	2250.00	2.30	25.00
Z	37.75	23.13	5.24	1150.00	4.82	15.00

Statistical Analysis

The data in this paper is presented as mean \pm SEM. We used Prism (GraphPad) and Excel (Microsoft) to perform statistical analysis. Statistical significance was calculated using one-way analysis of variance (ANOVA) followed by Tukey's multi-group comparisons or Fisher's LSD multiple comparisons. Groups were identified statistically different at $P < 0.05$. When the P -value was greater than 0.05, it is considered as non-significant (ns).

Declarations

Acknowledgments

We thank Zhong Chen and Weiwei Hu for providing CX3CR1-GFP mice, Qianqian Xin for helpful discussions, Lingxiao Gao and Yiming Rong for assistance in revising the manuscript, Jianxiong Zhang for help in figures editing.

Funding

This work was supported in part by the National Natural Science Foundation of China (61735016, 81771877), Natural Science Foundation of Zhejiang Province (LR20F050002), Key R&D Program of Zhejiang Province (2020C03009, 2021C03001), Zhejiang leading innovation and entrepreneurship team (202099144), CAMS Innovation Fund for Medical Sciences (2019-I2M-5-057), Fundamental Research Funds for the Central Universities.

Author contributions

W.G., K.S., and X.-K.X. conceived the concept. X.-K.X., X.-T.L., and Y.C. performed the experiments. X.-K.X., J.Z., S.G., and X.X. analyzed the data. X.-K.X., Y.X., X.L., and Y.Z. wrote the manuscript. K.S. and W.G. directed the study.

Competing interests

The authors declare that they have no competing interests.

Data and materials availability

All data needed to evaluate the conclusions in the paper are present in the paper and/or the Supplementary Materials. Source data are provided with this paper.

References

- Andoh, M., & Koyama, R. (2021). Assessing Microglial Dynamics by Live Imaging. *Front Immunol*, *12*, 617564. doi:10.3389/fimmu.2021.617564
- Bernier, L. P., York, E. M., Kamyabi, A., Choi, H. B., Weiling, N. L., & MacVicar, B. A. (2020). Microglial metabolic flexibility supports immune surveillance of the brain parenchyma. *Nat Commun*, *11*(1), 1559. doi:10.1038/s41467-020-15267-z
- Bruttger, J., Karram, K., Wortge, S., Regen, T., Marini, F., Hoppmann, N., . . . Waisman, A. (2015). Genetic Cell Ablation Reveals Clusters of Local Self-Renewing Microglia in the Mammalian Central Nervous System. *Immunity*, *43*(1), 92-106. doi:10.1016/j.immuni.2015.06.012
- Cangalaya, C., Stoyanov, S., Fischer, K. D., & Dityatev, A. (2020). Light-induced engagement of microglia to focally remodel synapses in the adult brain. *Elife*, *9*. doi:10.7554/eLife.58435
- Chamorro, Á., Dirnagl, U., Urra, X., & Planas, A. M. (2016). Neuroprotection in acute stroke: targeting excitotoxicity, oxidative and nitrosative stress, and inflammation. *The Lancet Neurology*, *15*(8), 869-881. doi:10.1016/s1474-4422(16)00114-9

- Cherry, J. D., Olschowka, J. A., & O'Banion, M. K. (2014). Neuroinflammation and M2 microglia: the good, the bad, and the inflamed. *J Neuroinflammation*, *11*, 98. doi:10.1186/1742-2094-11-98
- Cortes-Canteli, M., Kruyer, A., Fernandez-Nueda, I., Marcos-Diaz, A., Ceron, C., Richards, A. T., . . . Fuster, V. (2019). Long-Term Dabigatran Treatment Delays Alzheimer's Disease Pathogenesis in the TgCRND8 Mouse Model. *J Am Coll Cardiol*, *74*(15), 1910-1923. doi:10.1016/j.jacc.2019.07.081
- Cruz Hernandez, J. C., Bracko, O., Kersbergen, C. J., Muse, V., Haft-Javaherian, M., Berg, M., . . . Schaffer, C. B. (2019). Neutrophil adhesion in brain capillaries reduces cortical blood flow and impairs memory function in Alzheimer's disease mouse models. *Nat Neurosci*, *22*(3), 413-420. doi:10.1038/s41593-018-0329-4
- Cserep, C., Posfai, B., Lenart, N., Fekete, R., Laszlo, Z. I., Lele, Z., . . . Denes, A. (2020). Microglia monitor and protect neuronal function through specialized somatic purinergic junctions. *Science*, *367*(6477), 528-537. doi:10.1126/science.aax6752
- Davalos, D., Grutzendler, J., Yang, G., Kim, J. V., Zuo, Y., Jung, S., . . . Gan, W. B. (2005). ATP mediates rapid microglial response to local brain injury in vivo. *Nat Neurosci*, *8*(6), 752-758. doi:10.1038/nn1472
- Davalos, D., Ryu, J. K., Merlini, M., Baeten, K. M., Le Moan, N., Petersen, M. A., . . . Akassoglou, K. (2012). Fibrinogen-induced perivascular microglial clustering is required for the development of axonal damage in neuroinflammation. *Nat Commun*, *3*, 1227. doi:10.1038/ncomms2230
- Ding, G., Li, X., Lin, W., Kimochi, Y., & Sudo, R. (2017). Enhanced flocculation of two bioflocculation-producing bacteria by secretion of *Philodina erythropthalma*. *Water Res*, *112*, 208-216. doi:10.1016/j.watres.2017.01.044
- Dudvarski Stankovic, N., Teodorczyk, M., Ploen, R., Zipp, F., & Schmidt, M. H. H. (2016). Microglia-blood vessel interactions: a double-edged sword in brain pathologies. *Acta Neuropathol*, *131*(3), 347-363. doi:10.1007/s00401-015-1524-y
- Eles, J. R., Vazquez, A. L., Snyder, N. R., Lagenaur, C., Murphy, M. C., Kozai, T. D. Y., & Cui, X. T. (2017). Neuroadhesive L1 coating attenuates acute microglial attachment to neural electrodes as revealed by live two-photon microscopy. *Biomaterials*, *113*, 279-292. doi:10.1016/j.biomaterials.2016.10.054
- Fan, J. L., Rivera, J. A., Sun, W., Peterson, J., Haeberle, H., Rubin, S., & Ji, N. (2020). High-speed volumetric two-photon fluorescence imaging of neurovascular dynamics. *Nat Commun*, *11*(1), 6020. doi:10.1038/s41467-020-19851-1
- Fernandez-Lopez, D., Faustino, J., Klibanov, A. L., Derugin, N., Blanchard, E., Simon, F., . . . Vexler, Z. S. (2016). Microglial Cells Prevent Hemorrhage in Neonatal Focal Arterial Stroke. *J Neurosci*, *36*(10), 2881-2893. doi:10.1523/JNEUROSCI.0140-15.2016

- Fu, R., Shen, Q., Xu, P., Luo, J. J., & Tang, Y. (2014). Phagocytosis of microglia in the central nervous system diseases. *Mol Neurobiol*, *49*(3), 1422-1434. doi:10.1007/s12035-013-8620-6
- Fumagalli, S., Ortolano, F., & De Simoni, M. G. (2014). A close look at brain dynamics: cells and vessels seen by in vivo two-photon microscopy. *Prog Neurobiol*, *121*, 36-54. doi:10.1016/j.pneurobio.2014.06.005
- Gelosa, P., Lecca, D., Fumagalli, M., Wypych, D., Pignieri, A., Cimino, M., . . . Sironi, L. (2014). Microglia is a key player in the reduction of stroke damage promoted by the new antithrombotic agent ticagrelor. *J Cereb Blood Flow Metab*, *34*(6), 979-988. doi:10.1038/jcbfm.2014.45
- Greenhalgh, A. D., David, S., & Bennett, F. C. (2020). Immune cell regulation of glia during CNS injury and disease. *Nat Rev Neurosci*, *21*(3), 139-152. doi:10.1038/s41583-020-0263-9
- Haynes, S. E., Hollopeter, G., Yang, G., Kurpius, D., Dailey, M. E., Gan, W. B., & Julius, D. (2006). The P2Y₁₂ receptor regulates microglial activation by extracellular nucleotides. *Nat Neurosci*, *9*(12), 1512-1519. doi:10.1038/nn1805
- Hines, D. J., Hines, R. M., Mulligan, S. J., & Macvicar, B. A. (2009). Microglia processes block the spread of damage in the brain and require functional chloride channels. *Glia*, *57*(15), 1610-1618. doi:10.1002/glia.20874
- Hu, X., Leak, R. K., Shi, Y., Suenaga, J., Gao, Y., Zheng, P., & Chen, J. (2015). Microglial and macrophage polarization-new prospects for brain repair. *Nat Rev Neurol*, *11*(1), 56-64. doi:10.1038/nrneurol.2014.207
- Hu, X., Li, P., Guo, Y., Wang, H., Leak, R. K., Chen, S., . . . Chen, J. (2012). Microglia/macrophage polarization dynamics reveal novel mechanism of injury expansion after focal cerebral ischemia. *Stroke*, *43*(11), 3063-3070. doi:10.1161/STROKEAHA.112.659656
- Jolivel, V., Bicker, F., Biname, F., Ploen, R., Keller, S., Gollan, R., . . . Schmidt, M. H. H. (2015). Perivascular microglia promote blood vessel disintegration in the ischemic penumbra. *Acta Neuropathol*, *129*(2), 279-295. doi:10.1007/s00401-014-1372-1
- Lim, T. K., & Ruthazer, E. S. (2021). Microglial trophocytosis and the complement system regulate axonal pruning in vivo. *Elife*, *10*. doi:10.7554/eLife.62167
- Liu, L., Kearns, K. N., Eli, I., Sharifi, K. A., Soldo, S., Carlson, E. W., . . . Tvrđik, P. (2021). Microglial Calcium Waves During the Hyperacute Phase of Ischemic Stroke. *Stroke*, *52*(1), 274-283. doi:10.1161/STROKEAHA.120.032766
- Lou, N., Takano, T., Pei, Y., Xavier, A. L., Goldman, S. A., & Nedergaard, M. (2016). Purinergic receptor P2RY₁₂-dependent microglial closure of the injured blood-brain barrier. *Proc Natl Acad Sci U S A*, *113*(4), 1074-1079. doi:10.1073/pnas.1520398113

- Lubart, A., Benbenishty, A., Har-Gil, H., Laufer, H., Gdalyahu, A., Assaf, Y., & Blinder, P. (2021). Single Cortical Microinfarcts Lead to Widespread Microglia/Macrophage Migration Along the White Matter. *Cereb Cortex*, *31*(1), 248-266. doi:10.1093/cercor/bhaa223
- Marinov, T. M., & Santamaria, F. (2014). Computational modeling of diffusion in the cerebellum. *Prog Mol Biol Transl Sci*, *123*, 169-189. doi:10.1016/B978-0-12-397897-4.00007-3
- Mastorakos, P., Mihelson, N., Luby, M., Burks, S. R., Johnson, K., Hsia, A. W., . . . McGavern, D. B. (2021). Temporally distinct myeloid cell responses mediate damage and repair after cerebrovascular injury. *Nat Neurosci*, *24*(2), 245-258. doi:10.1038/s41593-020-00773-6
- Masuda, T., Croom, D., Hida, H., & Kirov, S. A. (2011). Capillary blood flow around microglial somata determines dynamics of microglial processes in ischemic conditions. *Glia*, *59*(11), 1744-1753. doi:10.1002/glia.21220
- Mendes, M. S., Le, L., Atlas, J., Brehm, Z., Ladron-de-Guevara, A., Matei, E., . . . Majewska, A. K. (2021). The role of P2Y12 in the kinetics of microglial self-renewal and maturation in the adult visual cortex in vivo. *Elife*, *10*. doi:10.7554/eLife.61173
- Merlini, M., Rafalski, V. A., Rios Coronado, P. E., Gill, T. M., Ellisman, M., Muthukumar, G., . . . Akassoglou, K. (2019). Fibrinogen Induces Microglia-Mediated Spine Elimination and Cognitive Impairment in an Alzheimer's Disease Model. *Neuron*, *101*(6), 1099-1108 e1096. doi:10.1016/j.neuron.2019.01.014
- Moskowitz, M. A., Lo, E. H., & Iadecola, C. (2010). The science of stroke: mechanisms in search of treatments. *Neuron*, *67*(2), 181-198. doi:10.1016/j.neuron.2010.07.002
- Nayak, D., Roth, T. L., & McGavern, D. B. (2014). Microglia development and function. *Annu Rev Immunol*, *32*, 367-402. doi:10.1146/annurev-immunol-032713-120240
- Neumann, J., Riek-Burchardt, M., Herz, J., Doeppner, T. R., Konig, R., Hutten, H., . . . Gunzer, M. (2015). Very-late-antigen-4 (VLA-4)-mediated brain invasion by neutrophils leads to interactions with microglia, increased ischemic injury and impaired behavior in experimental stroke. *Acta Neuropathol*, *129*(2), 259-277. doi:10.1007/s00401-014-1355-2
- Nimmerjahn, A., Kirchhoff, F., & Helmchen, F. (2005). Resting Microglial Cells Are Highly Dynamic Surveillants of Brain Parenchyma in Vivo. *Science*, *308*(5726), 1314-1318. doi:10.1126/science.1110647
- Nishimura, N., Schaffer, C. B., Friedman, B., Tsai, P. S., Lyden, P. D., & Kleinfeld, D. (2006). Targeted insult to subsurface cortical blood vessels using ultrashort laser pulses: three models of stroke. *Nat Methods*, *3*(2), 99-108. doi:10.1038/nmeth844
- Oyler-Yaniv, A., Oyler-Yaniv, J., Whitlock, B. M., Liu, Z., Germain, R. N., Huse, M., . . . Krichevsky, O. (2017). A Tunable Diffusion-Consumption Mechanism of Cytokine Propagation Enables Plasticity in Cell-to-Cell Communication in the Immune System. *Immunity*, *46*(4), 609-620. doi:10.1016/j.immuni.2017.03.011

- Peleg, M., & Corradini, M. G. (2011). Microbial growth curves: what the models tell us and what they cannot. *Crit Rev Food Sci Nutr*, *51*(10), 917-945. doi:10.1080/10408398.2011.570463
- Prinz, M., Jung, S., & Priller, J. (2019). Microglia Biology: One Century of Evolving Concepts. *Cell*, *179*(2), 292-311. doi:10.1016/j.cell.2019.08.053
- Prinz, M., & Priller, J. (2014). Microglia and brain macrophages in the molecular age: from origin to neuropsychiatric disease. *Nat Rev Neurosci*, *15*(5), 300-312. doi:10.1038/nrn3722
- Qiu, Y. M., Zhang, C. L., Chen, A. Q., Wang, H. L., Zhou, Y. F., Li, Y. N., & Hu, B. (2021). Immune Cells in the BBB Disruption After Acute Ischemic Stroke: Targets for Immune Therapy? *Front Immunol*, *12*, 678744. doi:10.3389/fimmu.2021.678744
- Shih, A. Y., Blinder, P., Tsai, P. S., Friedman, B., Stanley, G., Lyden, P. D., & Kleinfeld, D. (2013). The smallest stroke: occlusion of one penetrating vessel leads to infarction and a cognitive deficit. *Nat Neurosci*, *16*(1), 55-63. doi:10.1038/nn.3278
- Summers, P. M., Hartmann, D. A., Hui, E. S., Nie, X., Deardorff, R. L., McKinnon, E. T., . . . Shih, A. Y. (2017). Functional deficits induced by cortical microinfarcts. *J Cereb Blood Flow Metab*, *37*(11), 3599-3614. doi:10.1177/0271678X16685573
- Szalay, G., Martinecz, B., Lenart, N., Kornyei, Z., Orsolits, B., Judak, L., . . . Denes, A. (2016). Microglia protect against brain injury and their selective elimination dysregulates neuronal network activity after stroke. *Nat Commun*, *7*, 11499. doi:10.1038/ncomms11499
- Tennant, K. A., & Brown, C. E. (2013). Diabetes augments in vivo microvascular blood flow dynamics after stroke. *J Neurosci*, *33*(49), 19194-19204. doi:10.1523/JNEUROSCI.3513-13.2013
- Umpierre, A. D., Bystrom, L. L., Ying, Y., Liu, Y. U., Worrell, G., & Wu, L. J. (2020). Microglial calcium signaling is attuned to neuronal activity in awake mice. *Elife*, *9*. doi:10.7554/eLife.56502
- Umpierre, A. D., & Wu, L. J. (2020). How microglia sense and regulate neuronal activity. *Glia*. doi:10.1002/glia.23961
- Wu, L. J., Vadakkan, K. I., & Zhuo, M. (2007). ATP-induced chemotaxis of microglial processes requires P2Y receptor-activated initiation of outward potassium currents. *Glia*, *55*(8), 810-821. doi:10.1002/glia.20500
- Xu, P. (2020). Analytical solution for a hybrid Logistic-Monod cell growth model in batch and continuous stirred tank reactor culture. *Biotechnol Bioeng*, *117*(3), 873-878. doi:10.1002/bit.27230
- Xu, S., Lu, J., Shao, A., Zhang, J. H., & Zhang, J. (2020). Glial Cells: Role of the Immune Response in Ischemic Stroke. *Front Immunol*, *11*, 294. doi:10.3389/fimmu.2020.00294

Zhang, Y., Bander, E. D., Lee, Y., Muoser, C., Schaffer, C. B., & Nishimura, N. (2020). Microvessel occlusions alter amyloid-beta plaque morphology in a mouse model of Alzheimer's disease. *J Cereb Blood Flow Metab*, 40(10), 2115-2131. doi:10.1177/0271678X19889092

Zhou, K., Zhong, Q., Wang, Y. C., Xiong, X. Y., Meng, Z. Y., Zhao, T., . . . Yang, Q. W. (2017). Regulatory T cells ameliorate intracerebral hemorrhage-induced inflammatory injury by modulating microglia/macrophage polarization through the IL-10/GSK3beta/PTEN axis. *J Cereb Blood Flow Metab*, 37(3), 967-979. doi:10.1177/0271678X16648712

Figures

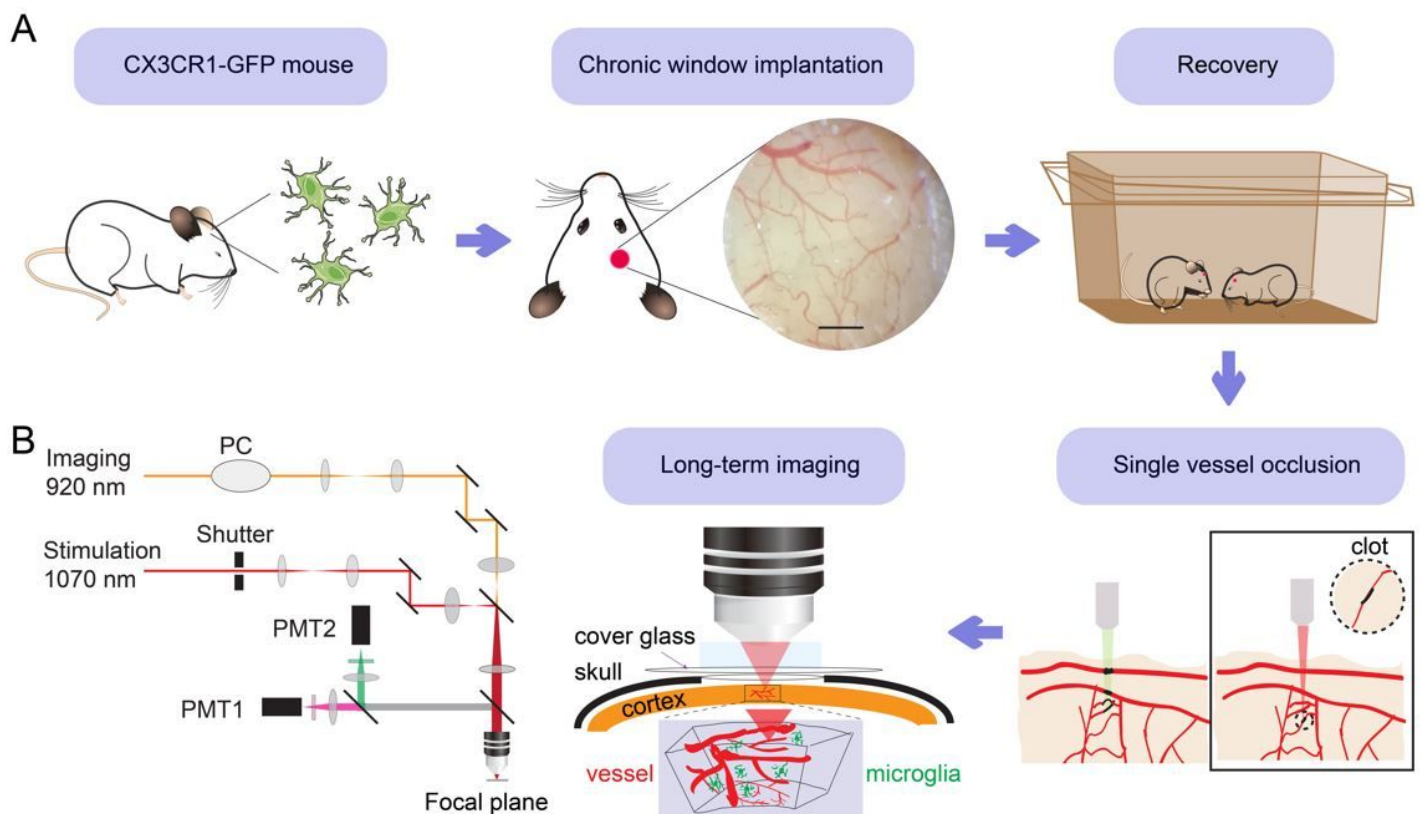
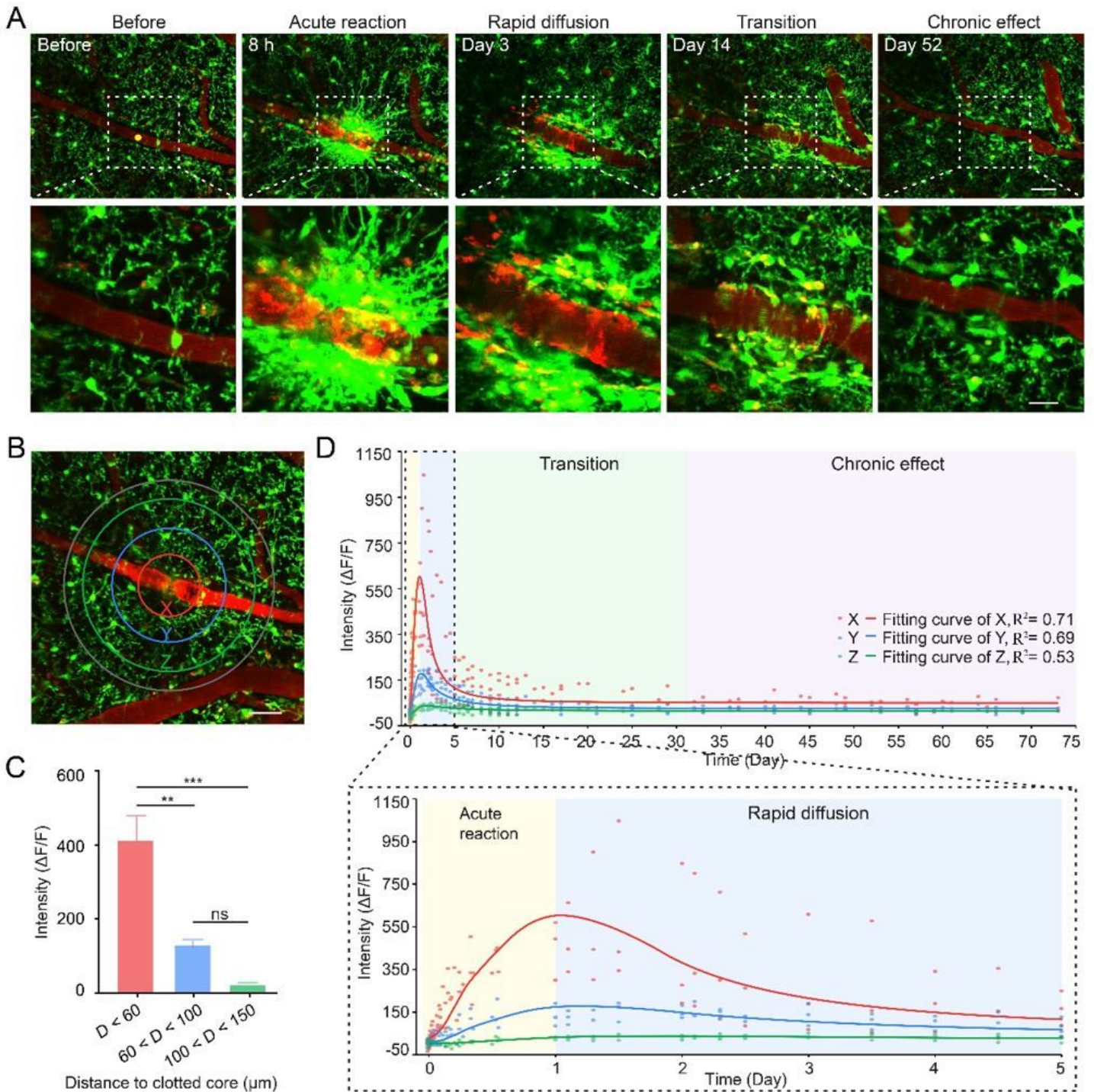


Figure 1

Experimental setup (A) Flowchart for the experimental procedure. CX3CR1-GFP mice were used for all experiments. After chronic window implantation was accomplished, mice were housed for about 4-weeks recovery from the surgery. Then with two-photon laser stimulation (right), single vessel occlusion was established (indicated by the dashed line). By comparison, conventional photothrombosis (left) causes all vessels within the light irradiation volume blocked (indicated by the black-colored blood vessels). Next, we performed real-time in vivo imaging of blood vessels and microglia by TPLSM through the specific cranial window. (B) Schematic of the two-photon laser scanning microscope modified for laser-induced occlusion and imaging simultaneously. PC, Pockels cell; PMT, photomultiplier tubes.



baseline. Scale bar, 50 μm . (C) Relative intensity quantification of different areas at 24 h after occlusion. D represents distance to the clotted core ($n = 4$ mice, $**P < 0.01$, $***P < 0.001$, ns indicates no significant difference, one-way ANOVA followed by Tukey's multiple comparison). Error bars, mean and SEM. (D) Scatterplot showing relative intensity quantification as shown in (B), $n = 4$ mice. Fitting curves show changing tendency of fluorescence intensity over time. Different colors shadow represents different phases. Boxed region indicates magnified view of dotted line.

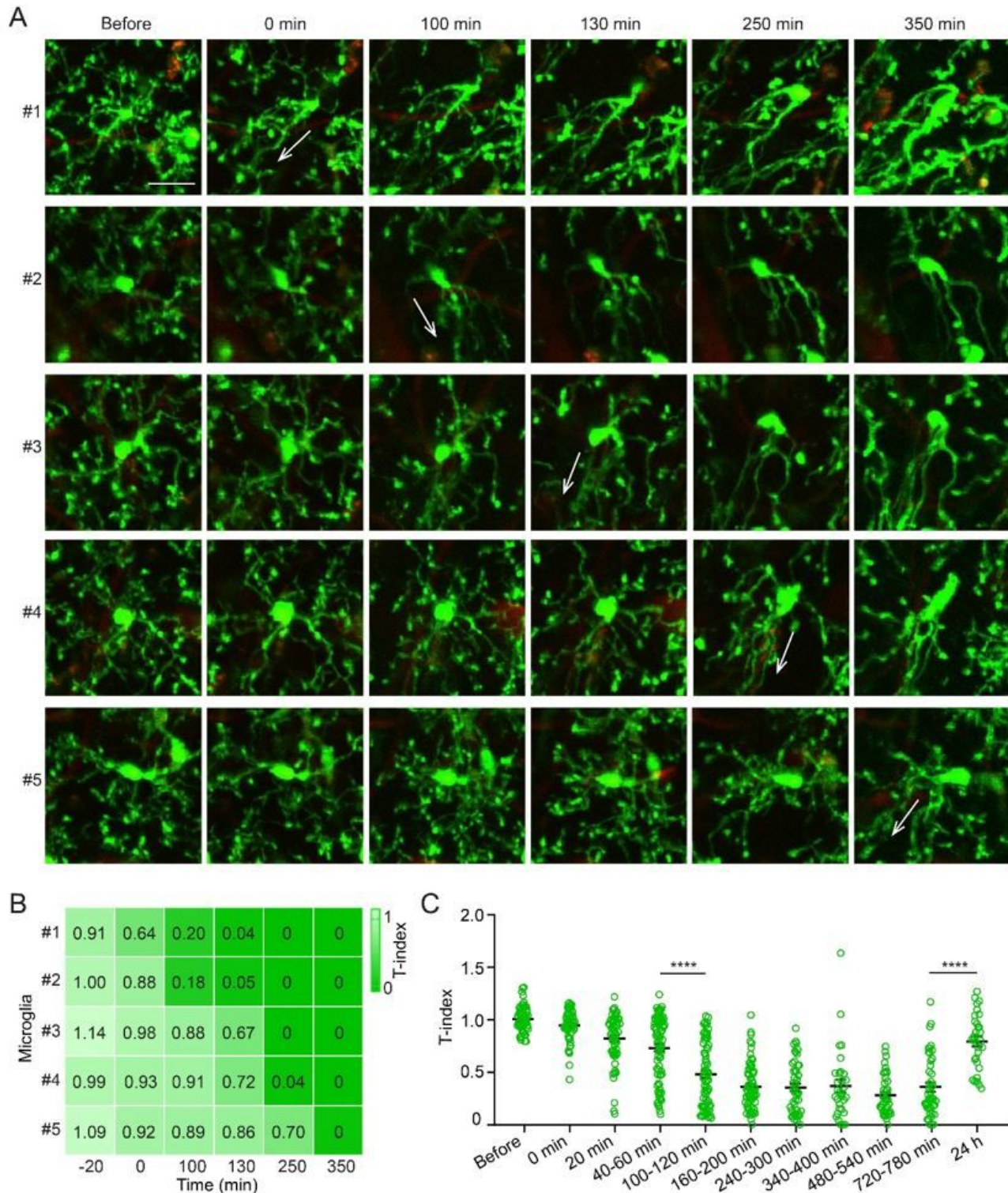


Figure 3

Microglia morphology dynamics in the acute reaction phase (A) Microglia processes facing occlusion site elongate, non-occlusion facing process retract. Images show morphology changes of five microglia from near to far away from the occlusion site at different time points. Their location was as shown in Supplementary Figure 5A. Arrows indicate the direction and the time at which microglia processes facing the vessel occlusion site elongate. Scale bar, 20 μ m. (B) T-index heatmap of five microglia shown in (A). The values of T-index at different time points are displayed. (C) Quantification of T-index during 24 h in response to occlusion (n = 4 mice, ****P < 0.0001, one-way ANOVA followed by Tukey's multiple comparison). Error bars, mean and SEM.

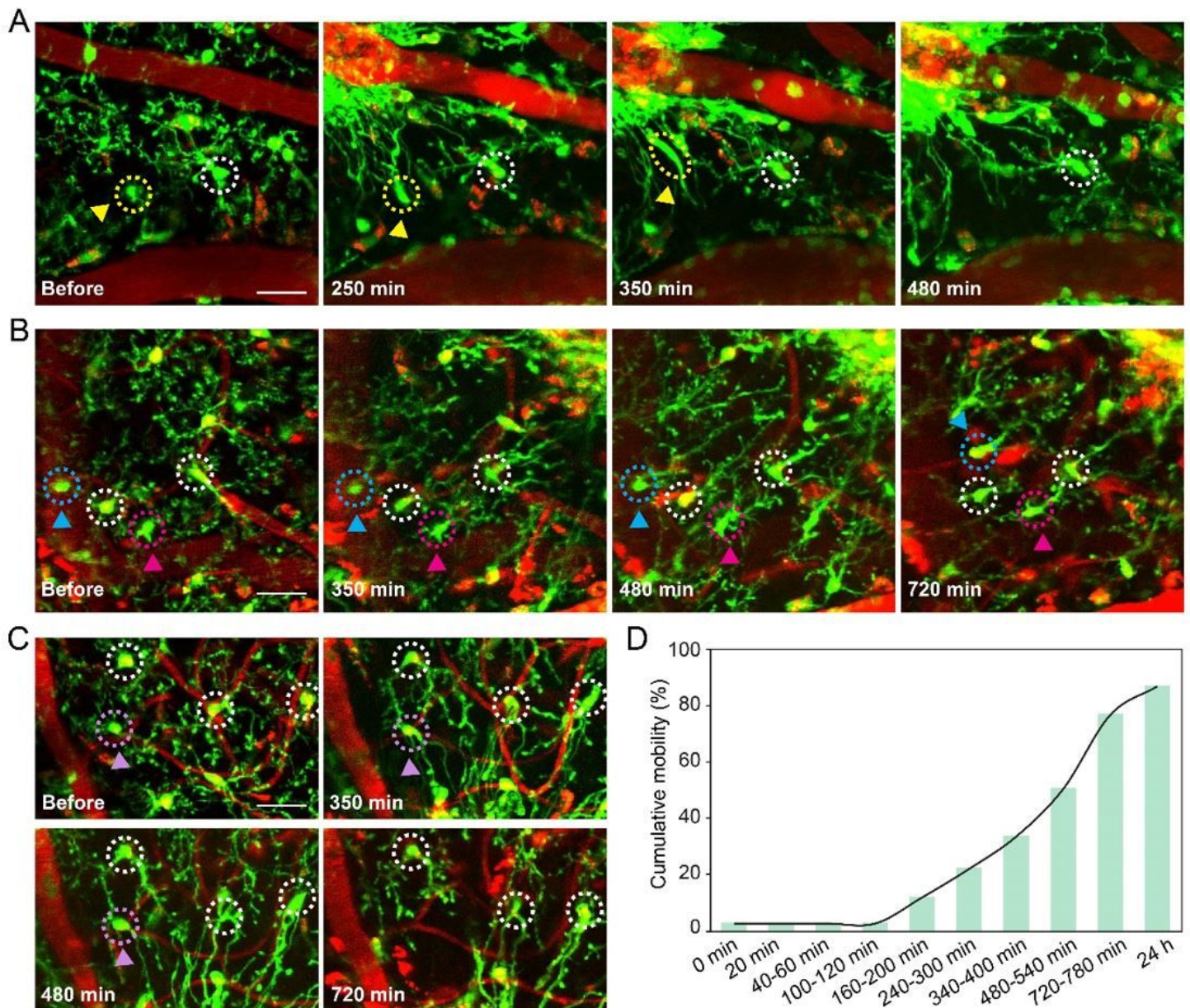


Figure 4

Microglial cumulative motility in the acute reaction phase (A) Microglial cell body changes from round shape to filamentous-like shape and follows the filamentary path to get into occlusion core. Yellow

arrowheads and dashed circles indicate representative microglia that underwent filamentous change. White dashed circle indicates stationary microglia. Scale bar, 30 μm . (B) Cyan and rosy arrowheads and dashed circles showing microglia with no filamentous deformation of the cell body migrating toward occlusion core. White dashed circle indicates stationary microglia. Scale bar, 30 μm . (C) Purple arrowheads and dashed circles indicate disappeared microglia with no migration occurrence. White dashed circle indicates stationary microglia. Scale bar, 30 μm . (D) Cumulative mobility of microglia in response to occlusion during 24 h. Data are plotted as mean value, $n = 4$ mice.

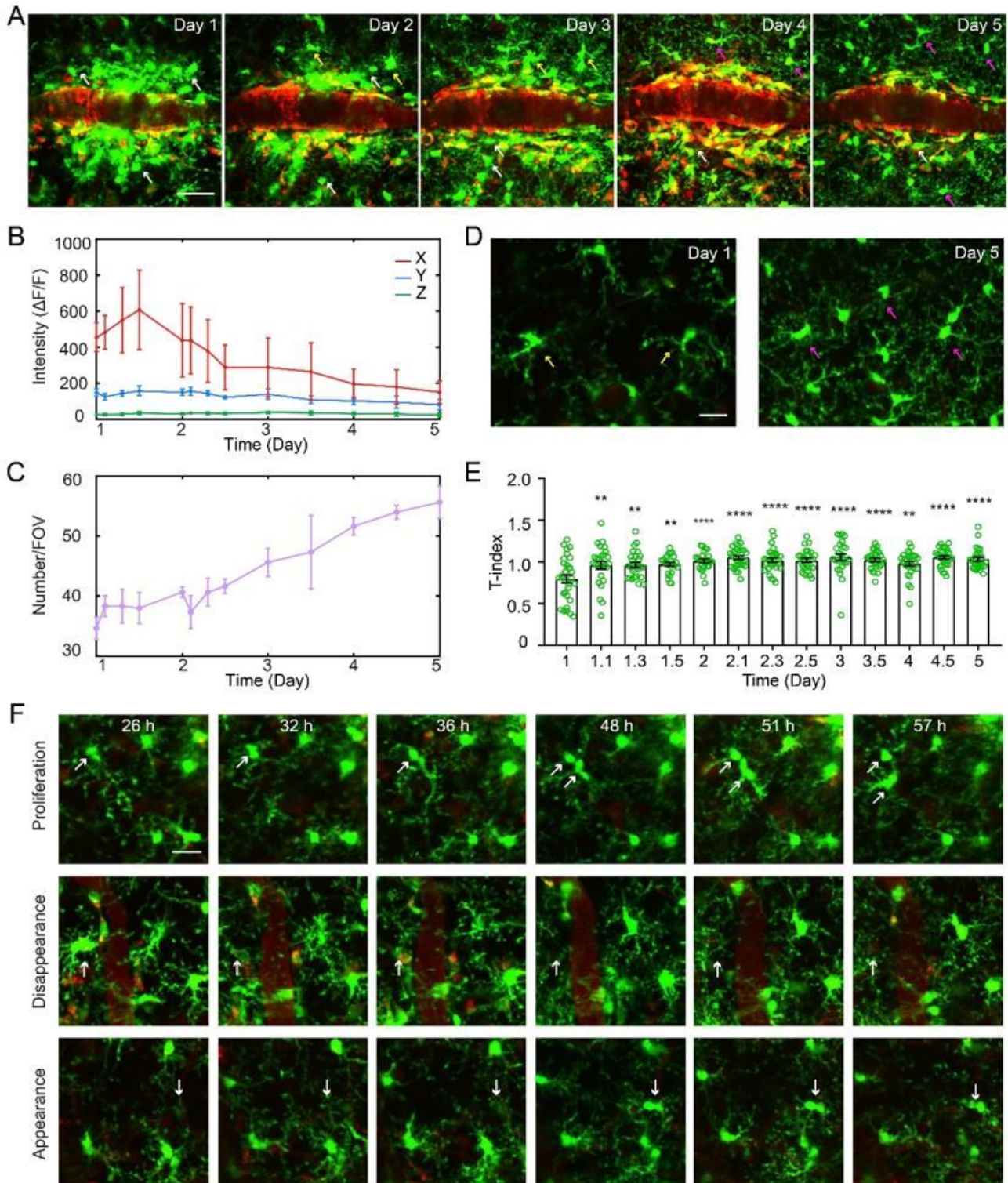


Figure 5

Microglia dynamics in the rapid diffusion phase (A) Repetitive in vivo imaging in the same FOV after occlusion shows a resolving microglia cluster over time. White arrows indicate microglia of round shape with few processes. Yellow arrows indicate microglia with asymmetric processes. Purple arrows indicate microglia with well-proportioned ramified process. Scale bar, 40 μm . (B) Persistent relative intensity variance at different time points from the inner to the outer area as shown in Figure 2B (n = 3 mice). Data are plotted as mean \pm SEM. (C) The number variance of microglia from day 1 to day 5 after occlusion (n = 3 mice). Data are plotted as mean \pm SEM. (D) Images showing difference in the number and morphology of microglia at day 1 and day 5 after occlusion. Compared with that at day 1 (yellow arrows), the symmetry of microglia process is significantly improved at day 5 (purple arrows). Scale bar, 20 μm . (E) Quantification of T-index at different time points (n = 3 mice, ** P < 0.01, ****P < 0.0001 versus T-index on day 1, one-way ANOVA followed by Tukey's multiple comparison). Error bars, mean and SEM. (F) Images showing proliferative microglia, disappeared microglia and appearance microglia during repeated imaging. Scale bar, 20 μm .

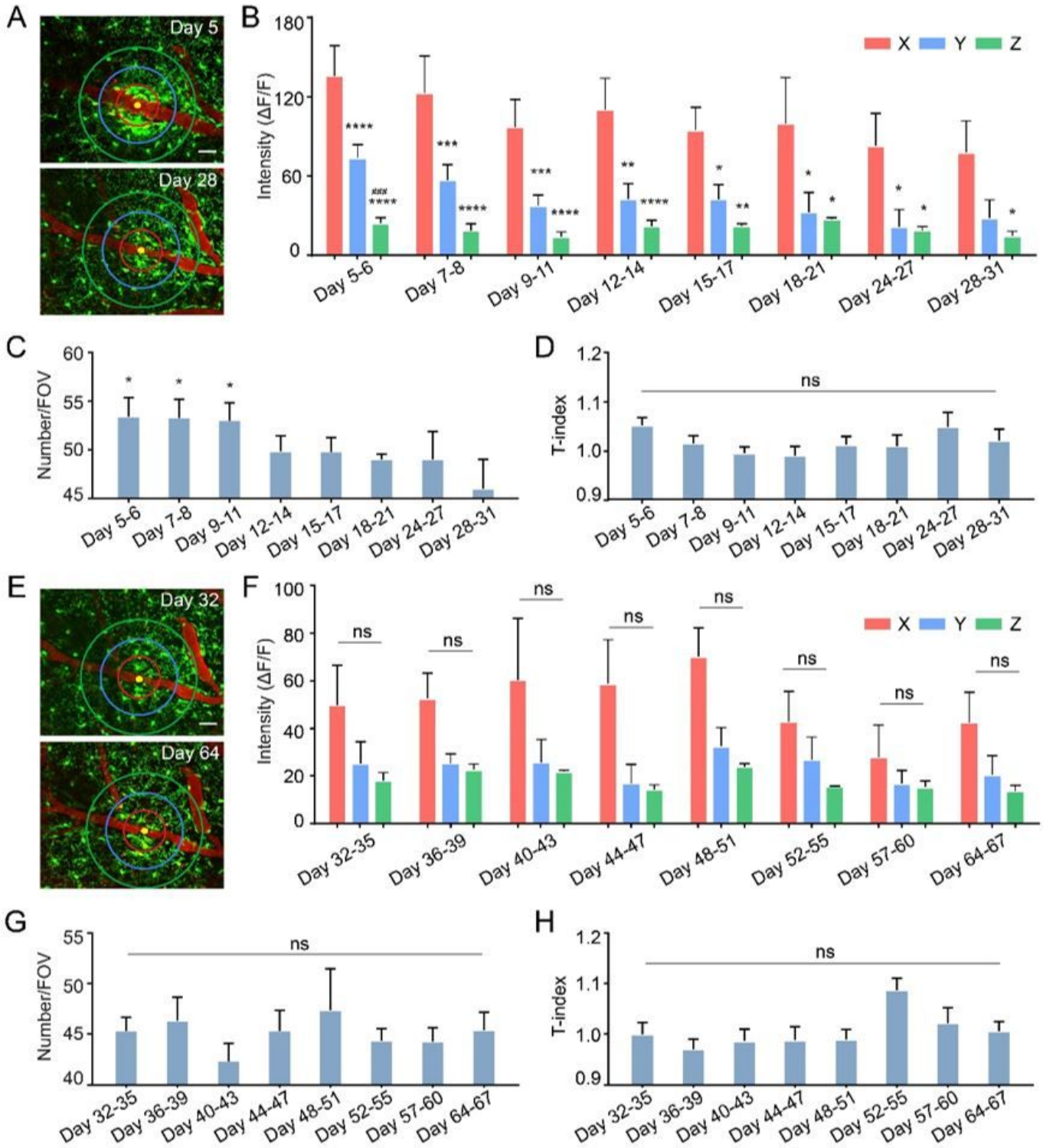


Figure 6

Microglia dynamics in the transition phase and chronic phase (A) Representative images in the transition phase. Scale bar, 40 μm . (B) Quantification of relative fluorescence intensity over time from the inner to the outer area as shown in Figure 2B (n = 3 mice, ### P < 0.001 versus Y; *P < 0.05, **P < 0.01, ***P < 0.001, ****P < 0.0001 versus X, one-way ANOVA followed by Fisher's LSD multiple comparison). (C) Time-course analysis of microglia number in the transition phase (n = 3 mice, *P < 0.05 versus day 28-31, one-

way ANOVA followed by Fisher's LSD multiple comparison). (D) Quantification of T-index in the transition phase (n = 3 mice, ns indicates no significant difference, one-way ANOVA followed by Tukey's multiple comparison). (E) Representative images in the chronic phase. Scale bar, 40 μ m. (F) Quantification of relative fluorescence intensity in the chronic phase from the inner to the outer area as shown in Figure 2B (n = 3 mice, ns indicates no significant difference, one-way ANOVA followed by Fisher's LSD multiple comparison). (G) Time-course analysis of microglia number in the chronic phase (n = 3 mice, ns indicates no significant difference, one-way ANOVA followed by Fisher's LSD multiple comparison). (H) Quantification of T-index in the chronic phase (n = 3 mice, ns indicates no significant difference, one-way ANOVA followed by Tukey's multiple comparison). Data are presented as mean and SEM.

Supplementary Files

This is a list of supplementary files associated with this preprint. Click to download.

- [sourcedata20211105.xlsx](#)
- [SupplementaryMaterials.docx](#)